Supplemental Material: Non-equilibrium diffusion of dark excitons in atomically thin semiconductors

Roberto Rosati,[1] Koloman Wagner,[2] Samuel Brem,[1] Raül Perea-Causín,[3] Jonas D. Ziegler,[2] Jonas Zipfel,[2] Takashi Taniguchi,[4] Kenji Watanabe,[5] Alexey Chernikov,[2] and Ermin Malic[1,3]

[1]*Department of Physics, Philipps-Universität Marburg, Renthof 7, D-35032 Marburg, Germany*
[2]*Department of Physics, University of Regensburg, Regensburg D-93053, Germany*
[3]*Chalmers University of Technology, Department of Physics, 412 96 Gothenburg, Sweden*
[4]*International Center for Materials Nanoarchitectonics, National Institute for Materials Science, Tsukuba, Ibaraki 305-004, Japan*
[5]*Research Center for Functional Materials, National Institute for Materials Science, Tsukuba, Ibaraki 305-004, Japan*

1. THEORETICAL METHODS

The excitonic landscape is calculated microscopically by solving the Wannier equation [1, 2]

$$\frac{\hbar^2 k^2}{2m_v}\Psi_v(\mathbf{k}) - \sum_{\mathbf{q}} W_{\mathbf{q}}\Psi_v(\mathbf{k}+\mathbf{q}) = E_v^{\mathrm{b}}\Psi_v(\mathbf{k}) \quad , \tag{1}$$

where E_v^{b} is the exciton binding energy and m_v the reduced exciton mass in the exciton valley. Single-particle energies and effective masses are obtained from first-principles calculations [3]. Furthermore, $\Psi_v(\mathbf{k})$ describes the excitonic wave function in momentum space, while $W_{\mathbf{q}} = V_q/\epsilon_{scr}(q)$ is the Coulomb potential for charges in a thin film of thickness d surrounded by a dielectric environment. It is determined by the bare 2D-Fourier transformed Coulomb potential V_q and a non-local screening [4]

$$\epsilon_{scr}(q) = \kappa_1 \tanh\left(\frac{1}{2}\left[\alpha_1 d q - \ln\left(\frac{\kappa_1-\kappa_2}{\kappa_1+\kappa_2}\right)\right]\right), \tag{2}$$

where $\kappa_i = \sqrt{\epsilon_i^{\parallel}\epsilon_i^{\perp}}$ and $\alpha_i = \sqrt{\epsilon_i^{\parallel}/\epsilon_i^{\perp}}$ account for the parallel and perpendicular component of the dielectric tensor ϵ_i of monolayer (i = 1) [5] and environment (i = 2) [6]. The solution of Eq. (1) provides us with a set of excitonic states and associated energies. Based on these, we can study the excitonic transport via Wigner representation [7, 8], providing in particular Eq. (1) of the main manuscript. Note that the latter holds in the low excitation regime, while at higher exciton densities Auger scattering and associated local heating can take place, resulting in the formation of halos [9–11]. Due to large spectral separations, we focus on the energetically lowest $1s$ states of the three most relevant exciton valleys (KK, KK′ and KΛ). Furthermore, we focus on the PL stemming from momentum-dark excitons, while spin-dark states require spin-flip processes and are thus expected to have a minor influence on the considered spatiotemporal exciton dynamics.

Extending the generalized Elliott formula introduced in [12] and adapted for time-resolved photoluminescence (PL) in [13], we can determine the spatiotemporally-resolved PL

$$I(E,\mathbf{r},t) = \frac{8|M|^2}{\hbar}\frac{I_0(E,\mathbf{r},t) + \sum_v I_v(E,\mathbf{r},t)}{4\left(E-E_{\mathrm{KK}}\right)^2 + \left(\gamma + \Gamma_0^{\mathrm{out,KK}}\right)^2}, \tag{3}$$

where $I_0(E,\mathbf{r},t) = \gamma N_0^{\mathrm{KK}}/2$ provides the direct radiative recombination term, while

$$I_v(E,\mathbf{r},t) = \sum_{\mathbf{Q},v,\beta,\pm} |D^v_{\beta;\mathbf{Q}}|^2 \eta_{\beta,\pm} N^v_{\mathbf{Q}}(E,\mathbf{r},t) \frac{2\Gamma^{\mathrm{out},v}_{\mathbf{Q}}}{4\left(E^v_{\mathbf{Q}} \pm \epsilon_\beta - E\right)^2 + \left(\Gamma^{\mathrm{out},v}_{\mathbf{Q}}\right)^2}$$

provides the indirect phonon-assisted PL. Here, M describes the excitonic optical matrix elements [2, 14], the indices $\pm$ and β refer to the emission/absorption of a phonon in the mode β and energy ϵ_β and inducing an exciton-phonon coupling $D^v_{\beta;\mathbf{Q}}$. Based on $I_v(E,\mathbf{r},t)$ one can define a set of effective diffusion coefficients $D_{E,v} = \frac{1}{2}\partial_t \sigma^2_{E,v}$, where $\sigma^2_{E,v}(t) = \int \mathbf{r}^2 I_v(E,\mathbf{r},t)d\mathbf{r}/2\int I_v(E,\mathbf{r},t)d\mathbf{r}$ is the squared standard deviation of the spatiotemporal distribution $I_v(E,\mathbf{r},t)$ for given v and E. Analogously one can define $D_E = \frac{1}{2}\partial_t\sigma^2_E$, where σ^2_E is the spatial width of the total PL.

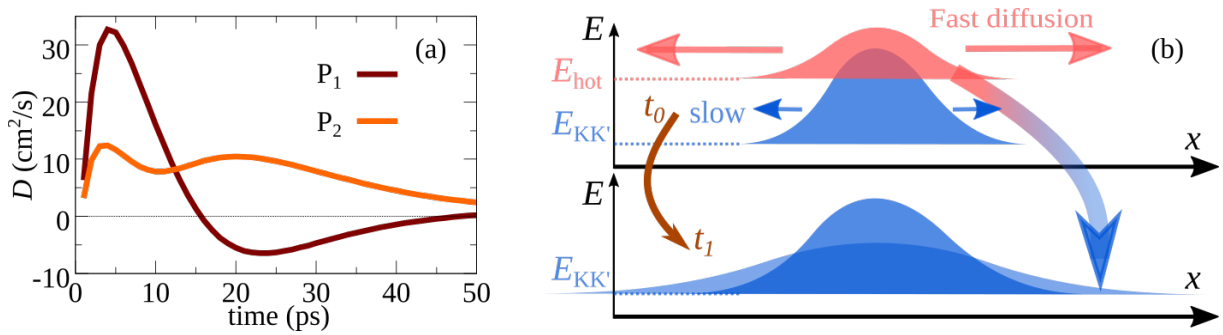

Fig. S 1. (a) Effective diffusion coefficient at phonon-sideband energies P_1 and P_2. (b) Sketch showing how hot exciton thermalization produces a bump in the diffusion coefficient of P_2.

2. VALLEY- AND ENERGY-RESOLVED EFFECTIVE DIFFUSION COEFFICIENTS

In Fig. S1(a) we show the evolution of the effective diffusion coefficients D_{P_1} and D_{P_2} at the energies of the phonon sidebands P_1 and P_2, cf. Fig. 2 in the main manuscript. The quick spatial broadening of P_1 as shown in Fig. 3(a) of the main manuscript is directly reflected in a steep increase of the diffusion coefficient D_{P_1} reaching values as high as 35 cm^2/s. The steep increase is followed by a quick decrease, showing also transient negative diffusion coefficients [15]. The origin of the high diffusion values can be traced back to hot excitons in the KK′ valley (rather than KΛ excitons, cf. discussion on Fig. S2). Higher effective diffusion coefficients are often followed by negative values as a consequence e.g. of inter- and intravalley exciton thermalization [15].

In contrast, the maximum value reached by D_{P_2} is approximately three times smaller, since at the energy $E \equiv P_2$ there are no PL contributions from hot excitons. Nevertheless, the latter can still affect the evolution of D_{P_2} in an indirect way, as reflected by the bump at approximately 20 ps. The origin of the bump is the thermalization of hot KK′ excitons, cf. Fig. S1(b). Soon after the optical excitation (top panel), hot and cold excitons in the same valley (red and blue area, respectively) have the same spatial width (provided by the optical excitation). However, the hot excitons diffuse faster and hence show a larger spatial broadening than cold excitons (bottom panel). Once they thermalize into the valley minimum via intravalley scattering, the spatial distribution of cold excitons suddenly becomes larger resulting in the bump observed in Fig. S1(a). Note that in case of a faster thermalization (e.g. at higher temperatures) or slower diffusion (e.g. for broader initial spatial distributions, cf. Fig. S3), we do not see such a bump, since cold and hot excitons have similar spatial distributions when the latter thermalize.

Fig. S2(a) shows the theoretically predicted effective diffusion coefficients as a function of energy and time. The diffusion at P_2 is dominated by cold KK′ excitons located at the valley minimum, while at higher energies hot excitons take over resulting in much higher diffusion coefficients (dark red regions). At energies around P_1, both cold

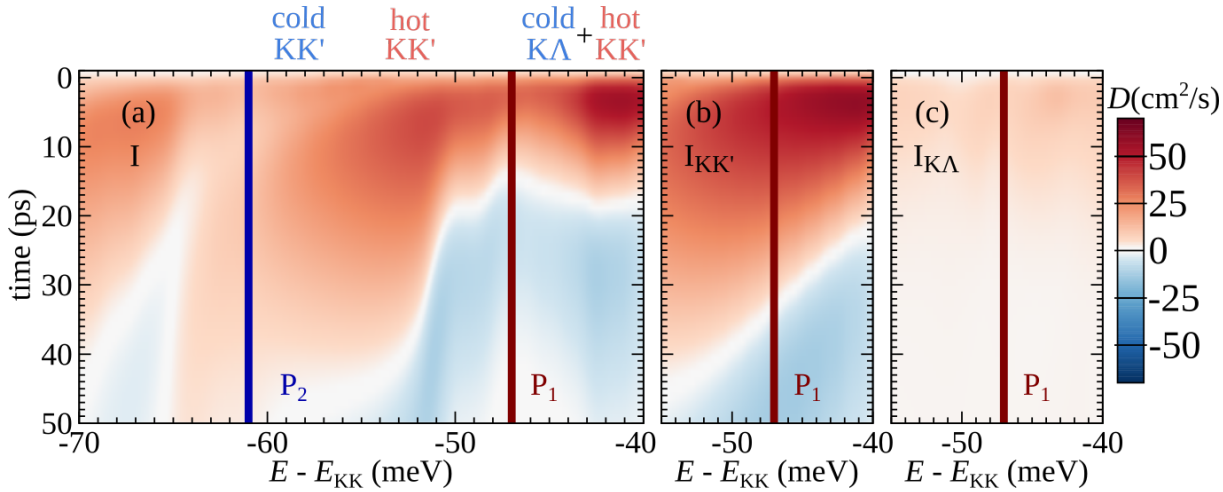

Fig. S 2. Energy-resolved effective diffusion coefficient of (a) $I(E, \mathbf{r}, t)$ and (b)-(c) focusing on the energy around P_1 and separating the contributions from $I_{KK'}(E, \mathbf{r}, t)$ and $I_{K\Lambda}(E, \mathbf{r}, t)$, respectively.

KΛ excitons populating the valley minimum as well as hot KK′ excitons contribute to the diffusion. To separate the two contributions, in Figs. S2(b-c) we consider only $I_{\mathrm{KK'}}(E,\mathbf{r},t)$ and $I_{\mathrm{K\Lambda}}(E,\mathbf{r},t)$, respectively. We observe very clearly that the initial fast diffusion (dark red regions) clearly stems from $I_{\mathrm{KK'}}$, i.e. hot KK′ excitons located approximately at the energy of $\mathrm{E_{K\Lambda}}$. The signal stemming from cold KΛ excitons shows approximately one order of magnitude smaller diffusion coefficients, cf. Fig. S2(c). Furthermore, the photoluminescence $I_{\mathrm{KK'}}(\mathrm{P}_1,\mathbf{r},t)$ shows a smoother and slower transition to negative diffusion coefficient values (Fig. S2(b)) compared to the total PL $I(\mathrm{P}_1,\mathbf{r},t)$ (Fig. S2(a)). The smooth transition is induced by the intravalley thermalization to lower energies, which is spatially non-uniform, since the occupation at lower energies are narrower in space due to slower effective diffusion, cf. Fig. S2(b). In contrast, the sharp decrease to negative values observed at approximately 10-15 ps around P_1 in Fig. S2(a) is the result of the competition between excitons being localized in different valleys and exhibiting different excess energies. In the first 15 ps, the P_1 signal is still dominated by hot KK′ excitons, hence the total PL $I(\mathrm{P}_1,\mathbf{r},t)$ shows a fast broadening (Fig. S2(a)) in accordance to the hot excitons in KK′ (Fig. S2(b)) and in contrast to the slow propagation of KΛ (Fig. S2(c)). Once hot KK′ excitons have cooled to energies below $E_{\mathrm{K\Lambda}}$ via intravalley scattering occurring within the first 10-15 ps at 20K, they are not able to contribute to P_1 any longer. As a result, the latter becomes dominated by cold KΛ excitons, which propagate slower in space. Thus, the relaxation of hot KK′ excitons to energies below $E_{\mathrm{K\Lambda}}$ results in a sharp decrease of the spatial width of excitons giving rise to the P_1 sideband (Fig. S2(a)).

3. DEPENDENCE ON INITIAL SPATIAL BROADENING

The faster diffusion of hot excitons results in spatially dependent occupations, i.e. hot excitons are more present in the spatial tails than at the center of the optically excited spatial distribution, cf. Fig 1(b). To study this we calculate spectrally-resolved PL at the center of an excitation pulse ($x = 0$) with a varying spatial width w. In Fig. S3(a) we show $I_{\Delta,0}(E,t)$ with $w \approx 0.5\mu$m as in the main manuscript. We find that the PL is initially ($t \lessapprox 10$ ps) dominated by the P_1 phonon sideband (red line), while at later stages the P_2 phonon sideband (blue line) becomes dominant. In the transient regime we observe a thermalization process of hot excitons initially formed approx. 15 meV above $E_{\mathrm{KK'}}$ [see Figs. 2(a-c) of main manuscript]. As they relax towards the minimum of KK′ excitons, the center of the corresponding PL shifts to the red (dashed arrow) resulting also in a transfer of the optical weight from P_1 to P_2.

Figures S3(b) and (c) illustrate the same study however now decreasing (increasing) the spatial width w of the initial spatial exciton distribution to $w/2$ ($2w$). In the case of a narrower distribution we observe a much weaker transient ($t \lessapprox 10$ ps) signal stemming from P_1 and a less pronounced relaxation process of hot exctions from P_1 to $\mathrm{P}_{K'}$ (cf. the thin dashed arrows). The reason for this behaviour lies in the interplay of the thermalization in energy and the diffusion in space. The narrower the exciton occupation, the larger its gradient and the faster is the diffusion, cf.

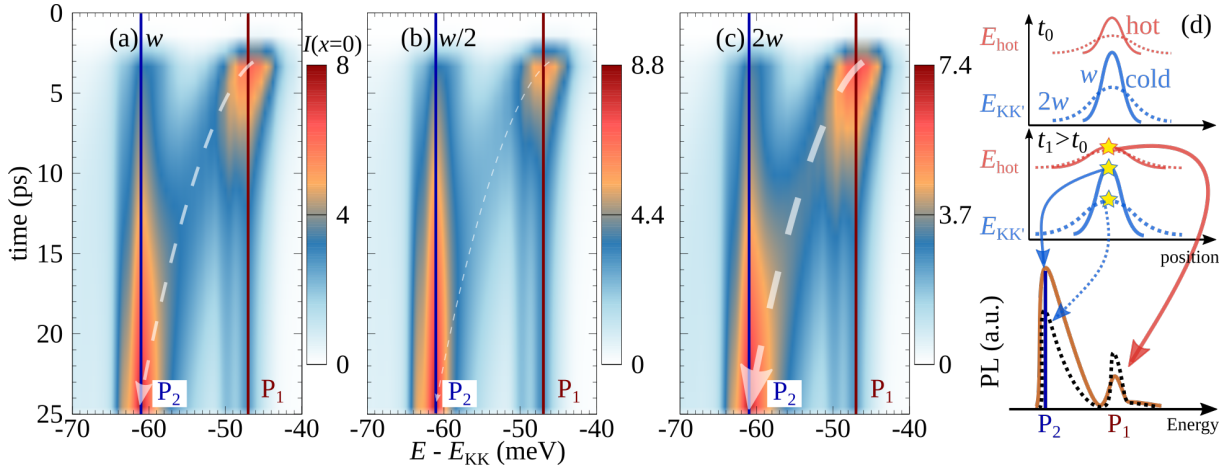

Fig. S 3. Energy- and time-resolved photoluminescence $I_{w,0}(E,t)$ coming from the center of an optical excitation $x = 0$ with spatial width (a) w (as in the main text), (b) $w/2$ and (c) $2w$. The PL has been normalized to $I(E_{\mathrm{KK}},x = 0,t)$ (with the colorbar maximum adjusted to the value of P_2 at 25 ps). (d) Sketch showing how a narrower spatial distribution (solid lines) provides a faster diffusion especially for hot excitons (red lines), while for a broader spatial distribution (dotted lines) hot and cold excitons show a similar broadening (upper panel). This results in a lower PL intensity for a narrower spatial distribution evaluated at $x = 0$ at P_1, which is initially ($t \lessapprox 10$ ps) dominated by hot excitons (bottom panel).

Fig. S3(d). This applies in particular to faster-diffusing hot excitons, while cold excitons with a small excess energy are less affected. Therefore, a smaller initial spatial width leads to a faster diffusion of hot excitons away from the center at $x = 0$, where their population becomes depleted. As a consequence, the phonon-assisted transient signal from hot excitons at e.g. P_1 is weaker compared to a larger initial w (solid vs dashed line in the bottom panel of Fig. S3(d)). The situation is reversed for an initially broader spatial distribution: Here the diffusion is weaker, hence spatial distributions of hot and cold excitons are similar (dotted lines in Figs. S3(d)). This results in a larger presence of hot excitons in $x = 0$, resulting in a larger transient signal at P_1, cf. Figs. S3(a,c).

Note that while the diffusion leads to a depletion of hot excitons from the center of the distribution $x = 0$, the opposite takes place in the spatial tail of the distribution, as hot excitons diffuse there from $x = 0$. In summary, hot excitons move away from the center of the optical excitation. This is particular true for narrower initial distributions, leading to a weaker corresponding spectrally-resolved emission from the center of the optical excitation.

4. LOW-TEMPERATURE EFFECTIVE DIFFUSION IN $MOSE_2$

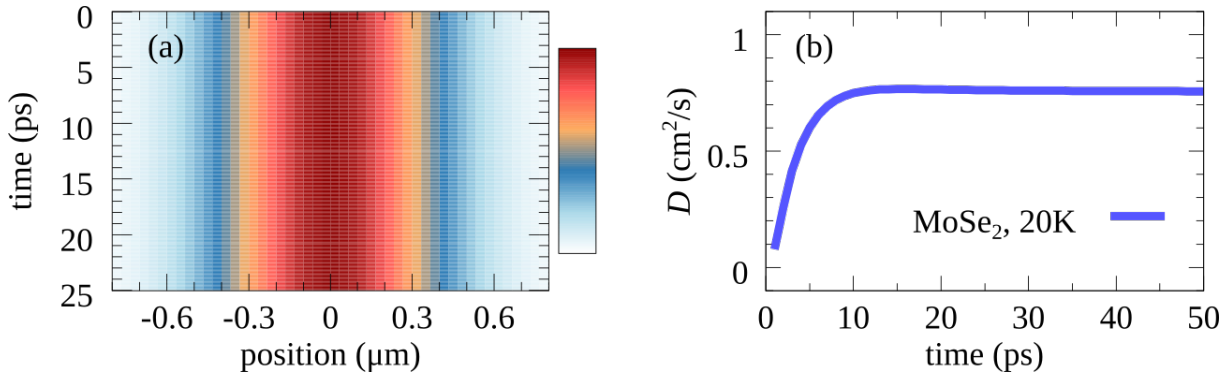

Fig. S4. (a) Spectrally-integrated PL in $MoSe_2$ at 20 K and (b) associated effective diffusion coefficient D displaying no onset of fast effective diffusion due to the absence of hot excitons.

While the speed-up of the effective diffusion in WSe_2 has been explained by hot excitons formed in the energetically lower-lying dark valleys, in Fig. S3 we show the behaviour in $MoSe_2$. Here KK is the energetically lowest valley, hence no dark hot excitons are initially formed. As a result, no initial speed-up of the energy integrated PL is observed in the first picoseconds (Fig. S3(a)), as revealed also by a quantitative analysis of the effective diffusion coefficient, Fig. S3(b). Here the maximum value coincides with the stationary one, in clear contrast with the case of WSe_2 where the two differed by an order of magnitude. The absence of initial fast effective diffusion in $MoSe_2$ shows once again that such a speed-up is as obtainable only in presence of dark valleys, where transient hot excitons are formed.

5. EXPERIMENTAL PHOTOLUMINESCENCE SPECTRA

In the main manuscript, the theoretically predicted fast diffusion of hot excitons is experimentally demonstrated by time- and spatially-resolved PL measurements on a hBN-encapsulated monolayer WSe_2. For an overview, a typical time-integrated, unpolarized luminescence spectrum of the studied sample at T = 5 K is shown in Fig. S5. Below the bright X_0 transition at almost 1.73 eV we observe a series of characteristic emission peaks. These include weak PL from negatively charged trion doublet about 30 meV below X_0 including an additional peak in-between, as well as the direct recombination from spin-dark excitons polarized in the out-of-plane direction and labeled as D_0. Below D_0 are several features originating from phonon-sideband emission of dark excitons in monolayer WSe_2. The most prominent resonance in this regime, about 60 meV below the bright exciton and labeled by P_2, represents phonon-assisted exciton recombination of momentum-indirect KK′ excitons[16, 17]. P_3 and P_{4++} were recently argued to stem from the phonon replicas of spin-dark KK [16] and momentum-indirect KK′ excitons under optical phonon emission, respectively [12, 13]. Finally, at energies around P_1 both hot KK′ and cold KΛ excitons should contribute to the emission [13].

For diffusion measurements the monolayer was resonantly excited at X_0 using a 100 fs Ti:sapphire laser. The PL signal was detected with a streak camera, providing both spatial and temporal resolution. Here, we focused on the diffusion of momentum-dark excitons by monitoring their phonon-assisted emission. To cut-off direct exciton

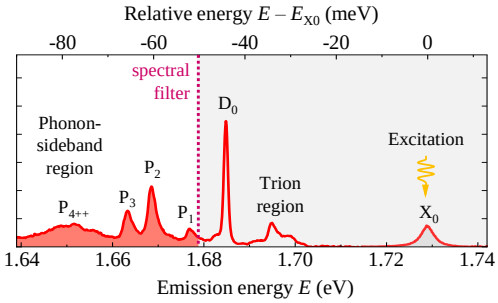

Fig. S 5. Time-integrated PL spectrum of a hBN-encapsulated WSe_2 monolayer at T = 5 K. Direct exciton recombination of bright and out-of-plane polarized spin-dark KK excitons is labeled by X_0 and D_0, respectively. Phonon sideband emission features are labeled by $P_1 - P_{4++}$. For the diffusion measurements the detected light was spectrally cut-off by a long-pass filter, blocking the PL indicated by the gray area.

recombination of the D_0, trion, and X_0 features, we used a spectral filter to detect only the phonon-sideband region, as indicated in Fig. S5

6. TRANSIENT DIFFUSION COEFFICIENT ESTIMATED FROM TIME-RESOLVED SPECTRA

Here, we illustrate the estimation of transient diffusion coefficients based on the time-dependent measurements of emission energies from the PL spectra. In the semi-classical description, that should be applicable at the studied temperature of 5 K, the diffusion coefficient D has the form:

$$D = \frac{\langle E_{kin} \rangle \tau_s}{M_x}. \tag{4}$$

It is proportional to the mean kinetic energy $\langle E_{kin} \rangle$ of the excitons, momentum scattering time τ_s, and the exciton total mass M_x. For an equilibrated exciton distribution the kinetic energy is given by the lattice temperature, i.e. $\langle E_{kin} \rangle = k_B T$. At non-equilibrium conditions, however, it can be approximated by adding an average excess energy ΔE. The latter can be estimated from the spectral analysis, since phonon-assisted processes allow for recombination of excitons with essentially arbitrary kinetic energies and momenta. Consequently, ΔE should essentially correspond to the relative shift of the phonon sideband emission energy with respect to the equilibrium value [13].

For the purpose of this analysis we consider time-resolved PL spectra of the phonon sidebands, obtained for circularly polarized resonant excitation and co-polarized detection. The data is reported in a previous study [13] and reproduced in Fig. S6(a). The emission in the spectral range between -45 and -65 meV with respect to X_0 largely stems from the phonon-assisted recombination of the momentum-dark KK′ excitons (c.f., P_1 and P_2 features in Fig. S5). For an exemplary illustration we neglect additional contributions from KΛ excitons with small excess energies that do not significantly influence fast initial diffusion. As discussed in the main manuscript and Ref. [13], the transient energy shift of the emission is a direct consequence of initially overheated exciton distribution of KK′ states that subsequently equilibrate and cool down over time. The energy of the shift of PL signal in this range, relative to the steady-state emission of the P_2 phonon sideband at -60 meV, thus roughly corresponds to the average excess energy ΔE of the KK′ excitons.

From the spectra, we determine the ΔE shift by evaluating the center of gravity, as illustrated in the exemplary data in the bottom panel of Fig. S6 (a). Here, we use the high energy cut-off of -50 meV corresponding to the conditions in the diffusion measurement. A constant offset is subtracted prior to the analysis and the resulting mean energy is marked by purple lines. The resulting the mean energy shift ΔE is presented as a function of time Fig. S6 (b). For the reference, we also include smaller and larger values for the high-energy cut-off. Diffusion coefficients presented in Fig. S6 (c) are then obtained via Eq. (4) by setting $\langle E_{kin} \rangle = \Delta E + k_B T$ using the ΔE values from Fig. S6 (b). We further set the momentum-scattering time τ_s to $\hbar/(0.235\,\text{meV}) = 2.8\,\text{ps}$, corresponding to the value for the exciton scattering with linear acoustic phonons, extracted from temperature-dependent linewidth broadening coefficient of 47 μeV/K. The exciton total mass of 0.75 m_0 is taken from the sum of the electron and hole masses in monolayer WSe_2 [3] and the lattice temperature is set to the heat-sink temperature of T = 5 K. Fig. S6(d) shows the resulting transient broadening of the spatial PL width assuming an initial Gaussian distribution with $w_0 = 0.5$ μm and $w^2 = w_0^2 + 4 \int \mathrm{D} dt$.

From this analysis, we indeed confirm the expectation of an initially rapid expansion of a hot exciton cloud with

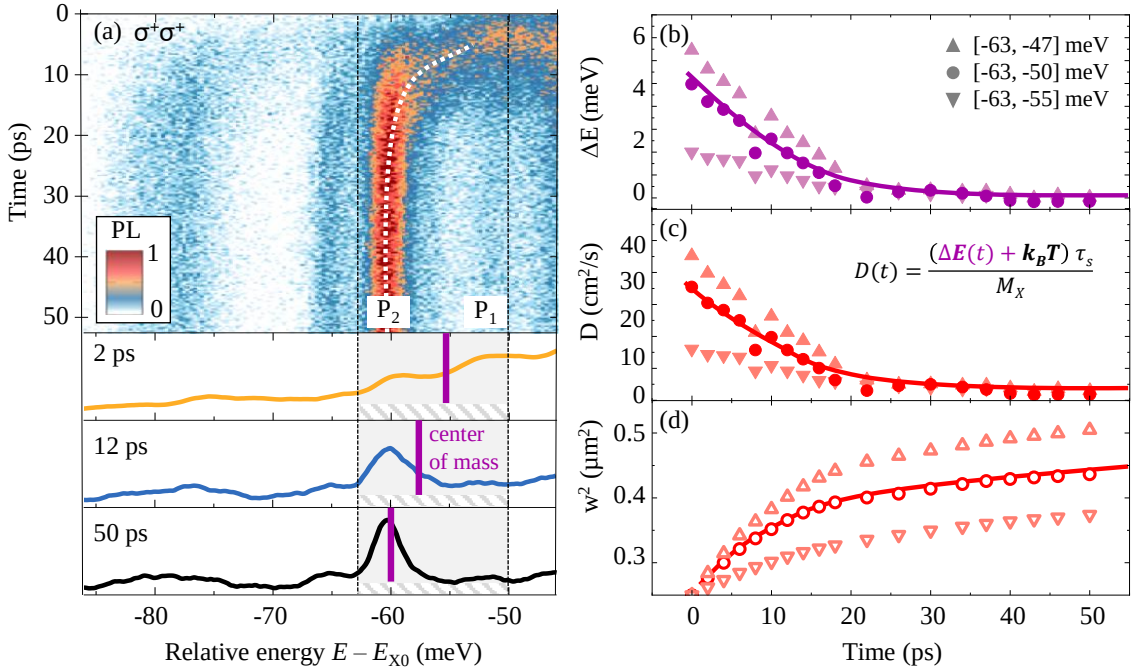

Fig. S 6. Transient diffusion coefficients from spectral energy shifts. (a) Experimental time- and energy-resolved PL spectra of a hBN-encapsulated WSe_2 monolayer at T = 5 K after circularly polarized, resonant excitation of X_0. Data is shown for co-polarized detection in the energy range where only phonon side bands contribute to the PL (taken from Ref. [13]). The dashed white line schematically illustrates the average energy shift ΔE with time. Lower panels show PL spectra at selected times. Purple lines indicate center of gravity within the selected energy range between −63 and −47 meV, as indicated by the gray area. (b) Extracted energy shifts ΔE(t) from (a) for several energy intervals with different values of the high-energy cut-off. (c) Corresponding transient diffusion coefficient D obtained via the semi-classical expression in Eq. 4 using parameters $\tau_s = 2.8$ ps and $M_x = 0.75 m_0$. (d) Resulting time-dependent broadening of the spatial profile for an initial spot width of $w \approx 0.5$ μm.

diffusion coefficients on the order of 20 to 40 cm^2/s at early times. Moreover, the equilibration time-scale of about 10 to 15 ps is very similar to both theoretical predictions and the decay of transient diffusivity in spatially-resolved measurements. As discussed in the main manuscript, such close quantitative agreement with direct measurements of the diffusion provides further support for the overall consistent interpretation of our observations.

[1] M. Selig, G. Berghäuser, A. Raja, P. Nagler, C. Schüller, T. F. Heinz, T. Korn, A. Chernikov, E. Malic, and A. Knorr, Nat. Commun. **7**, 13279 (2016).
[2] S. Brem, M. Selig, G. Berghaeuser, and E. Malic, Sci. Rep. **8**, 8238 (2018).
[3] A. Kormányos, G. Burkard, M. Gmitra, J. Fabian, V. Zólyomi, N. D. Drummond, and V. Fal'ko, 2D Mater. **2**, 022001 (2015).
[4] S. Brem, J. Zipfel, M. Selig, A. Raja, L. Waldecker, J. D. Ziegler, T. Taniguchi, K. Watanabe, A. Chernikov, and E. Malic, Nanoscale **11**, 12381 (2019).
[5] A. Laturia, M. L. Van de Put, and W. G. Vandenberghe, npj 2D Mater. Appl. **2**, 6 (2018).
[6] R. Geick, C. H. Perry, and G. Rupprecht, Phys. Rev. **146**, 543 (1966).
[7] O. Hess and T. Kuhn, Phys. Rev. A **54**, 3347 (1996).
[8] R. Jago, R. Perea-Causín, S. Brem, and E. Malic, Nanoscale **11**, 10017 (2019).
[9] M. Kulig, J. Zipfel, P. Nagler, S. Blanter, C. Schüller, T. Korn, N. Paradiso, M. M. Glazov, and A. Chernikov, Phys. Rev. Lett. **120**, 207401 (2018).
[10] R. Perea-Causín, S. Brem, R. Rosati, R. Jago, M. Kulig, J. D. Ziegler, J. Zipfel, A. Chernikov, and E. Malic, Nano Lett. **19**, 7317 (2019).
[11] J. Zipfel, M. Kulig, R. Perea-Causín, S. Brem, J. D. Ziegler, R. Rosati, T. Taniguchi, K. Watanabe, M. M. Glazov, E. Malic, and A. Chernikov, Phys. Rev. B **101**, 115430 (2020).
[12] S. Brem, A. Ekman, D. Christiansen, F. Katsch, M. Selig, C. Robert, X. Marie, B. Urbaszek, A. Knorr, and E. Malic, Nano Lett. **20**, 2849 (2020).

[13] R. Rosati, K. Wagner, S. Brem, R. Perea-Causín, E. Wietek, J. Zipfel, J. D. Ziegler, M. Selig, T. Taniguchi, K. Watanabe, A. Knorr, A. Chernikov, and E. Malic, ACS Photonics **7**, 2756 (2020).
[14] M. Selig, G. Berghäuser, M. Richter, R. Bratschitsch, A. Knorr, and E. Malic, 2D Mater. **5**, 035017 (2018).
[15] R. Rosati, R. Perea-Causín, S. Brem, and E. Malic, Nanoscale **12**, 356 (2020).
[16] E. Liu, J. van Baren, T. Taniguchi, K. Watanabe, Y.-C. Chang, and C. H. Lui, Phys. Rev. Res. **1**, 032007 (2019).
[17] M. He, P. Rivera, D. Van Tuan, N. P. Wilson, M. Yang, T. Taniguchi, K. Watanabe, J. Yan, D. G. Mandrus, H. Yu, H. Dery, W. Yao, and X. Xu, Nat. Commun. **11**, 618 (2020).